Machine Learning Techniques for Coherent CFAR Detection Based on Statistical Modeling of UHF Passive Ground Clutter

Nerea del-Rey-Maestre, María-Pilar Jarabo-Amores, David Mata-Moya, José-Luis Bárcena-Humanes, and Pedro Gómez del Hoyo

***Abstract*—Ultra high frequency (UHF) passive ground clutter statistical models were determined from real data acquired by a passive radar for the design of approximations to the Neyman–Pearson detector based on machine learning techniques. The cross-ambiguity function was the input space without any preprocessing. The Gaussian model was proved to be suitable for high Doppler values. Other models were proposed for Doppler close to zero, where ground clutter and low bistatic Doppler targets concentrate. Likelihood ratio detectors were built for this Doppler region, and a neural-network-based adaptive threshold technique was designed for fulfilling false alarm requirements throughout all the input space. The proposed scheme outperformed a conventional passive radar one and could be used as a reference for future designs.**

***Index Terms*—Machine learning, Neyman-Pearson, adaptive threshold, UHF passive ground clutter, statistical models, cross-ambiguity function, passive radar.**

I. Introduction

PASSIVE Radars (PR) are emerging technologies that encompass a set of techniques to detect targets and to estimate their positions and velocities, using non-cooperative signals (communications, radar, or radio-navigation signals) as Illuminators of Opportunity (IoO), rather than a dedicated transmitter [1]. System design and performance are strongly determined by the IoO (waveform, transmitted power, availability), and the geometry of the radar scenario.

Different IoOs have been studied in the last decades. Analog TV and FM radio were considered in [2] and [3], respectively, constituting basic references of PR technology. Systems based on Digital Video Broadcasting-Terrestrial (DVB-T) IoOs are under intensive research [4]–[10].

Manuscript received July 31, 2017; revised October 23, 2017; accepted November 22, 2017. Date of publication December 6, 2017; date of current version February 16, 2018. This work was supported in part by the Spanish "Ministerio de Economía y Competitividad" under Project TEC2015-71148-R and in part by the European FP7 Project FP7-COOPERATION-2013-SEC-SCOUT-607019. The guest editor coordinating the review of this manuscript and approving it for publication was Prof. Maria Sabrina Greco. *(Corresponding author: María-Pilar Jarabo-Amores.)*

The authors are with the Department of Signal Theory and Communications, Superior Polytechnic School, University of Alcalá, 28805 Alcalá de Henares, Spain (e-mail: nerea.rey@uah.es; mpilar.jarabo@uah.es; david.mata@uah.es; jose.barcena@uah.es; pedrojose.gomez@uah.es).

Color versions of one or more of the figures in this paper are available online at http://ieeexplore.ieee.org.

Digital Object Identifier 10.1109/JSTSP.2017.2780798

Main advantages of PRs compared to active radars are low cost due to the usage of Commercial Off-The-Shelf (COTS) components, smaller size, lower weight, lower probability of being intercepted, and minimisation of electromagnetic or environmental problems. Besides, PRs are not affected by the progressive spectrum occupancy of communication systems.

Drawbacks related to PRs are: a) out-of-control waveforms are used that are not designed according to detection purposes; b) the most suitable relative locations of IoOs and PRs cannot be always used; c) the transmitted power level and stability do not always fulfil the desirable requirements.

The radar detector has to decide between target absence (null hypothesis, H_0) and target presence (alternative hypothesis, H_1) in presence of the receiving chain thermal noise, the radar echoes generated by non-desired objects present in the area of coverage, clutter, and especially, the direct interference of the IoO signal, whose power is usually much higher that the target echo. The Neyman-Pearson (NP) detector maximizes the Probability of Detection (P_D) maintaining the Probability of False Alarm (P_{FA}) lower than or equal to a given value [11], [12]. If $\widetilde{\mathbf{z}}$ is the complex observation vector, and $f(\widetilde{\mathbf{z}}|H_0)$ and $f(\widetilde{\mathbf{z}}|H_1)$ are the likelihood functions, a possible implementation consists in comparing the Likelihood Ratio (LR), $\Lambda(\widetilde{\mathbf{z}})$, to a threshold, η_{lr}, estimated according to P_{FA} requirements (1) [12].

$$\Lambda(\widetilde{\mathbf{z}}) = \frac{f(\widetilde{\mathbf{z}}|H_1)}{f(\widetilde{\mathbf{z}}|H_0)} \underset{H_0}{\overset{H_1}{\gtrless}} \eta_{lr}(P_{FA}) \tag{1}$$

Some approximations to the NP detector apply adaptive cancelers for clutter filtering and Constant False Alarm Rate (CFAR) systems, many of which assume Gaussian interference models [13]–[16]. Solutions based on the Generalized Likelihood Ratio (GLR) were also considered [17]–[20].

The reciprocal filter approach was proposed in [21], and the DVB-T signal structure was exploited in [6] for the design of pre-processing stages to mitigate the effects of signal deterministic components and clutter in range-Doppler processing. In [22] different techniques based on sub-carrier orthogonality in OFDM (Orthogonal Frequency-Division Multiplexing) signals were compared and applied to a DVB-T based PR. The channel detector presented in [10] unifies clutter rejection and moving target detection, using the estimated impulse response of the Doppler channel.

As alternatives, learning machines trained in a supervised manner using a suitable error function were proved to be able to approximate the NP detector [23], [24]: Multi-Layer Perceptrons (MLP), [25], Radial Basis Function Neural Networks (RBFNN) [26], Second Order Neural Networks (SONN) [27], Support Vector Machines (SVM) [28], [29].

Nowadays, there is a general trend toward cognitive radars. Three main properties of cognitive radars are [30]: "1) intelligent signal processing, which builds on learning through interactions of the radar with the surrounding environment; 2) feedback from the receiver to the transmitter, which is a facilitator of intelligence; and 3) preservation of the information content of radar returns, which is realized by the Bayesian approach to target detection through tracking." In passive radars, the feedback from the receiver to the transmitter is not possible, but an intelligent algorithm capable of selecting the most suitable IoO among those available in the radar scenario can be designed and implemented [31].

In this context, the radar scene analyser is the cognitive radar main element responsible of the characterization of the radar scenario. It should provide environment and target statistical information to the detection and tracking tasks [32]. One of the objectives of this paper is to demonstrate that the knowledge about the statistical characterization of the radar returns can be used to design machine learning based detectors, exploiting the concept of cognition in passive radars.

Numerous measurement campaigns have been carried out for decades to obtain data of ground and sea clutter using active radars, so as to characterise their statistical distributions. The statistical characteristics of clutter depend on frequency, polarisation, incidence and scattering directions, and system resolution. The Gaussian model is widely used in low resolution radars (pulse width $> 0.5\,\mu$s and grazing angles $> 5^\circ$ for monostatic sea clutter). It is also considered when the grazing angle is $> 5^\circ$, regardless of radar resolution, for land clutter. In high resolution radars, the Probability Density Function (PDF) of clutter exhibits a long tail ('spiky' clutter), and the study of alternative clutter statistical distributions is required [33].

On the contrary, very few studies of bistatic clutter are available in the literature. They were mainly made using radar frequencies, and the results cannot be easily extrapolated to communication systems frequencies used in many passive radars. A study with bistatic sea clutter in the C band was carried out in [34], measuring the bistatic reflection coefficient (σ^0, the cross section per unit area). A study in the L band was presented in [35]. Measurements of σ^0 from L band to X band for terrain clutter were carried out in [36]. A detailed analysis of the published radar data, and the proposal of an empirical model, which expresses the variation of $E\{\sigma^0\}$ with the measurement geometry and sea conditions, working in the X band, were carried out in [37]. All these works used raw radar data, acquired with active bistatic radars in different frequency bands, and without any preprocessing.

More recent papers were published dealing with FM frequencies [38]–[40], GSM (Global System for Mobile communications) [41], [42], S-band [43]–[47]. Nevertheless, as far as the authors know, there is not any study of clutter modelling with passive radars that use the DVB-T signal as IoO.

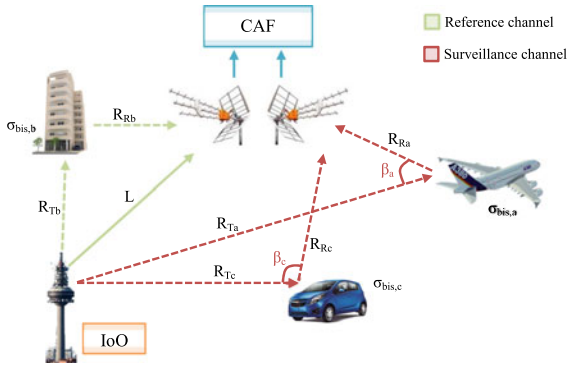

Fig. 1. Basic geometry of a bistatic PR. R_{Ti} is the target-to-transmitter distance, R_{Ri} is the target-to-receiver distance, L is the transmitter-to-receiver distance, β_i is the bistatic angle, and $\sigma_{bis,i}$ is the bistatic radar cross section (RCS), where $i \in \{b, c, a\}$ refers to *building*, *car*, and *airplane*, respectively.

Data acquired by a DVB-T passive radar demonstrator developed at the University of Alcalá [48], were used for clutter characterization and the design of detection schemes based on learning machines. IDEPAR central frequency can be varied from 450 MHz to 850 MHz, the signal bandwidth is equal to 25 MHz, and the maximum acquisition time is equal to 40 s. The output of the Cross Ambiguity Function (CAF) was the observation space, and amplitude, in-Phase (I) and in-Quadrature (Q) components, and complex samples ($\widetilde{\mathbf{z}}$) statistics were estimated. A semi-urban scenario composed of big buildings, vegetation and parking areas was considered. Results demonstrated that the Gaussian model can be applied in areas of the CAF far from the zero Doppler. However, a non-homogeneous characterisation was required for the region close to the zero Doppler. The proposed coherent clutter models were used for implementing a bank of LR detectors. Due to the complexity of the LRs, and its variability throughout the CAF, a learning machine was trained to implement the CFAR operation throughout the whole CAF, taking [49] as starting point. The proposed solution outperformed conventional PR detection schemes in clutter rejection and P_D.

The paper is structured as follows: in Section II the operating principle of PRs is summarized. The proposed approach is presented in Section III. Clutter models and statistical analysis techniques are studied in Section IV. In Section V, the radar scenario and the observation space parameters are defined. Statistical analysis results are presented in Section VI. The detection scheme based on the bank of LR detectors is designed in Section VII, and the machine learning based CFAR technique is designed and validated in Section VIII. Finally, the main conclusions are summarized in Section IX.

II. Passive Radar Principle

PRs detect and track objects by processing reflections from IoOs, such as commercial broadcast and communications signals. Due to the lack of control over the transmitter, a reference channel is used to acquire the signal transmitted by the IoO, and a surveillance one to capture targets echoes. The basic geometry and associated parameters are defined in Fig. 1, whilst the basic receiver architecture is presented in Fig. 2, which includes the following stages:

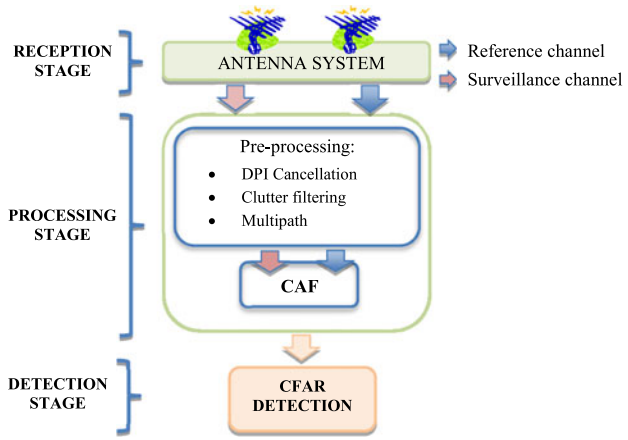

Fig. 2. Basic architecture of a PR.

– The reception stage is composed of the antenna system, radio frequency (RF) front-ends, and analog-to-digital converters (ADC), for generating digital reference and surveillance channels.
– The processing stage, which includes matched filtering and pre-processing techniques for rejecting interferences.
– Non-coherent CFAR techniques are usually applied in the detection stage.

For performing the matched filtering, delayed and Doppler shifted copies of the reference channel signal are correlated with the surveillance channel one to generate the Cross-Ambiguity Function (CAF) [3][2][50]:

$$S^{CAF}\left[m,p\right]=\sum_{n=0}^{N-1}s_{ref}^{*}\left[n-m\right]\cdot s_{surv}\left[n\right]\cdot\exp^{-j2\pi\frac{p}{N}n} \tag{2}$$

– $s_{ref}[n]$ is the reference signal.
– $s_{surv}[n]$ is the surveillance signal.
– $N=T_{int}\cdot f_s$, is the number of samples, being T_{int} (s) the integration time, and f_s (Hz) the sampling frequency.
– m is the time bin associated with a delay $\tau_m = m/f_s$.
– p is the Doppler-shift corresponding to $f_{dop}=f_s\,(p/N)$.

The CAF is based on the matched filter implementation which maximises the Signal to Noise Ratio (SNR), when Additive White Gaussian Noise (AWGN) is considered, and it is used by the vast majority of radars and communication systems [51]. Although this implementation is not optimum for detection when clutter is present, it is frequently used for several reasons [52]: It is simpler than the optimum receiver; clutter scattering function may be unknown, and it can work almost as well as the optimum receiver in many situations.

In radar signal design and analysis, the Ambiguity Function (AF) is a basic tool. It is calculated using (2) substituting $s_{surv}[n]$ by $s_{ref}[n]$. In PRs, the kind of IoO determines the detection properties. The DVB-T signal is composed of a random component and deterministic ones included for signal decoding in commercial TVs. Its AF is a thumbtack function with spurious, that spread throughout the delay-Doppler plane of the CAF [6], [53]. The study of these spurious is of great interest, and different solutions were proposed in the literature for reducing their impact on the system detection performance [8], [54], [55].

PR signal processing architectures usually include adaptive cancelers for clutter filtering before CAF generation, and Constant False Alarm Rate (CFAR) detectors (Fig. 2), many of which assume Gaussian interference models [13]–[16]. Solutions based on the Generalized Likelihood Ratio (GLR) have also been considered [17]–[20].

In [21], the reciprocal filter was proposed to keep the desired target delay and Doppler information after range-Doppler processing, getting rid of the autocorrelation of the reference signal. The filter performs a modulus frequency equalization of the transmitted signal. Because it is calculated from the actual measured reference signal, it can be applied to an arbitrary IoO waveform. In this line, the DVB-T signal structure was exploited for the design of reference and surveillance channels pre-processing techniques to reduce the impact of clutter and ambiguities [6]. In [22], different techniques based on subcarrier orthogonality in OFDM signals were compared. Clutter rejection and moving target detection were unified in the channel detector proposed in [10].

The problem of detecting a target in presence of noise, the direct IoO signal captured by the surveillance channel (DPI), clutter, and interfering targets in additive white Gaussian noise was also formulated as a composite hypothesis test [18]. Results proved that the basic architecture depicted in Fig. 2 is based on the GLR detector for no interfering targets and known noise variance. Both approaches differ in the method applied for estimating clutter complex amplitudes: in Fig. 2 adaptive filters are used for subtracting DPI and clutter from the surveillance channel before the CAF, in [18] the Maximum Likelihood Estimates, MLE, of clutter complex amplitudes are derived for all the clutter region in the delay-Doppler plane.

III. Proposed Methodology

When the CAF is applied to reference and surveillance signals without any preprocessing, the results are the MLEs of the complex amplitude, delay and Doppler shift of the desired targets and the clutter [56]. In this work, the CAF output is used as observation space for the detection problem formulation.

Neural Networks (NN) have been proposed for radar detection. In [23], a theoretical study proved that learning machines trained in a supervised manner using a suitable error function are able to approximate the NP detector. In this paper, an alternative approach is proposed, based on a detailed study of clutter statistics for determining statistical models to be used for the implementation of a bank of LR detectors, and a NN based CFAR technique for guaranteeing the desired P_{FA}.

For each scatterer, the result of the CAF is the AF of the transmitted signal, scaled and shifted to be centred on the scatterer time delay and Doppler shift. In Fig. 3 the CAFs generated by different combinations of the DPI and stationary point targets are compared. The main contributions concentrate on the zero Doppler line, with spreading effects of the main peaks, and pedestals that spread throughout all the Range-Doppler plane. Signal powers along a Doppler line far from zero were estimated

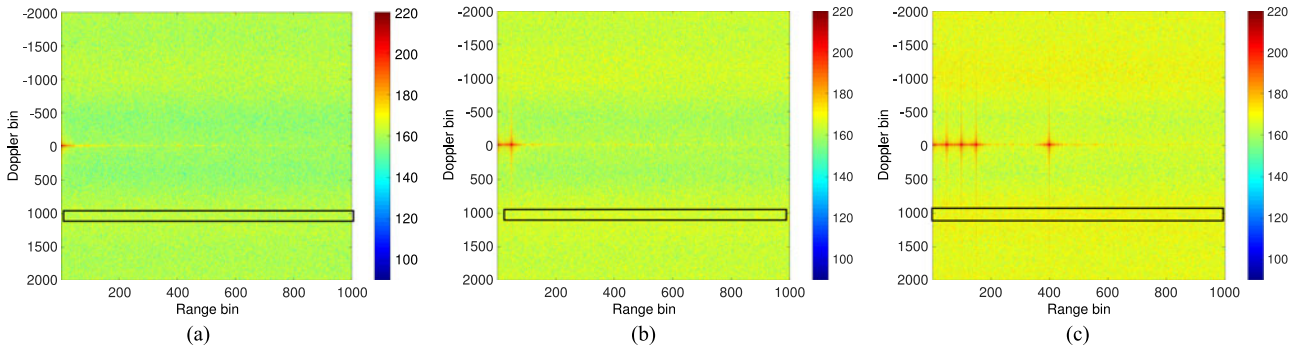

Fig. 3. CAF for the DPI (a), for a point stationary target plus the DPI (b), and for a set of four stationary targets plus the DPI (c). The average value of the magnitude of the samples belonging to the row marked with a black rectangle are: 163.28 dBW for (a), 166.24 dBW for (b), and 170.37 dBW for (c).

TABLE I
DISTRIBUTIONS FOR CLUTTER INTENSITY MODELING, $x = |\widetilde{\mathbf{z}}|^2$

Exponential **E**; $x \geq 0$	$f(x\|\lambda) = \lambda \cdot e^{-\lambda x}$; $\lambda > 0$
Weibull **W**; $x \geq 0$	$f(x\|a,\rho) = \frac{a \cdot x^{a-1}}{\rho^a} \cdot e^{-(x/\rho)^a}$ $a > 0, \rho > 0$; if $a = 1$, **E** with $\lambda = 1/\rho$ [41]
K-distributed **K**; $x \geq 0$	$f(x\|\nu,b) = \frac{2 \cdot b^{\frac{\nu+1}{2}} \cdot x^{\frac{\nu-1}{2}}}{\Gamma(\nu)} K_{\nu-1}(2\sqrt{xb})$ $\nu > 0, b > 0$; if $\nu \longrightarrow \infty$, **E**
Log-normal **LN**; $x \geq 0$	$f(x\|a,\mu) = \frac{1}{ax\sqrt{2\pi}} \cdot e^{\left(-\frac{(ln(x)-\mu)^2}{2a^2}\right)}$ $a > 0, \mu \in \Re$
Gamma Γ; $x \geq 0$	$f(x\|a,\nu) = \frac{1}{\Gamma(\nu)a^\nu} \cdot x^{\nu-1} \cdot e^{-\frac{x}{a}}$ $a > 0, \nu > 0$; if $\nu = 1$ and $a = 1/\lambda$, **E**
Gamma Mixture [61] ΓMD; $x \geq 0$	$f(x) = \sum_{j=1}^{k} w_j \cdot \phi(x\|\nu_j, a_j)$ $\phi(x\|\nu_j, a_j)$ is Γ, $w_j \geq 0$ and $\sum_{j=1}^{k} w_j = 1$

TABLE II
DISTRIBUTIONS FOR CLUTTER I/Q COMPONENTS MODELLNG

Normal **N**; $y \in \Re$	$f(y\|\mu,\sigma) = \frac{1}{\sigma\sqrt{2\pi}} \cdot e^{-\frac{(y-\mu)^2}{2\sigma^2}}$ $\mu \in \Re, \sigma > 0$
Logistic **LG**; $y \in \Re$	$f(y\|\mu,s) = \frac{e^{-(y-\mu)/s}}{s\left(1+e^{-\frac{y-\mu}{s}}\right)^2}$ $\mu \in \Re$, $s > 0$; if $s = \sigma\sqrt{3}/\pi$, **N**
Gaussian Mixture [62], [63] **GMD**; $y \in \Re$	$f(y) = \sum_{j=1}^{k} w_j \cdot \phi(y, \mu_j, \sigma_j)$ $\phi(y, \mu_j, \sigma_j)$ is **N**, $w_j \geq 0$, $\sum_{j=1}^{k} w_j = 1$

$y = \Re(\widetilde{\mathbf{z}})$ is the in-phase (I) component.

(caption of Fig. 3), showing an increase in the estimated power as the number of stationary point targets increases.

In a semi-urban scenario, big buildings are expected to generate strong CAF contributions similar to those presented in Fig. 3. Other clutter sources are cars in parking areas, trees, and urban furniture, in general. The proposed methodology includes a local study of different CAF regions for determining the likelihood functions, the implementation of a bank of LR detectors using the estimated likelihood functions, assuming a Gaussian target for H_1; and the design of a CFAR technique based on a NN for adaptively estimating the detection thresholds and guaranteeing the desired P_{FA} throughout the whole CAF.

IV. CLUTTER MODELS AND STATISTICAL ANALYSIS TECHNIQUES

The Gaussian model is applicable when the echo can be modelled as that from a number of independent, random scatterers, with no one individual scatterer producing an echo of magnitude commensurate with the resultant echo from all scatterers [57]. Large deviations from Gaussian statistics are observed in data acquired at low grazing angles and/or by high-resolution systems [58]. Tables I and II summarize the considered distributions. In the Weibull case, the relationships among intensity, (a,ρ), and amplitude, (ν,b), parameters are the following: $a = \nu/2$, $\rho = b^2$, beign $\nu > 0$ and $b > 0$ [59]. In the Log Normal, the shape and scale parameters for the amplitude, (σ,μ), are: $a = 2\sigma$, $b = 2\mu$, being $\mu \in \Re$ and $\sigma > 0$. Data statistical analysis was carried out comparing the Empirical Probability Density Function (EPDF) with the theoretical PDFs whose parameters were estimated applying the Method of Moments [60].

A. Goodness-of-Fit Tests

Goodness-of-fit tests based on the estimation of the distance between the empirical and theoretical Cumulative Distribution Functions (CDFs) are usually used to analyze the applicability of theoretical distributions [41], [42]. In this work, the two-sample Kolmogorov-Smirnov (KS-test2) and the two-sample Cramér-von-Mises (CM-test2) were applied [64]–[66].

Given two random vectors, $[X_1, ..., X_N]$ and $[Y_1, ..., Y_M]$, the KS-test2 and the CM-test2 are implemented as follows:

1) Evaluate the ECDF of both observation vectors: $\widehat{F}_X(x)$ and $\widehat{F}_Y(x)$.
2) Compute the statistic KS-distance, $d_{KS} = sup_x|\widehat{F}_X(x) - \widehat{F}_Y(x)|$, and CM-distance, $d_{CM} = \frac{NM}{(N+M)} \int_{-\infty}^{\infty} |\widehat{F}_X - (x)\widehat{F}_Y(x)|^2 dH(x)$, where sup is the supremum of the set of distances, and $H(x)$ is the empirical distribution function of the two samples together [66].
3) Compare the d_{KS} and d_{CM} with a threshold, selected according to the significance level, α, and the two sample sizes, N and M. If d_{KS} and d_{CM} exceed the

Fig. 4. Radar scenario with two IoOs: Torrespaña ($40°25'16.64''N$, $3°39'51.39''W$, at a height of 658 m) and Algete ($40°30'47.19''N$, $3°20'55.02''W$, at a height of 628 m). PR located on the flat roof of the Polytechnic School of the University of Alcalá ($40°30'46.97''N$, $3°20'55.42''W$, at a height of 628 m).

defined thresholds, H_0 will be rejected. Alternatively, if the $p-value$ is less than the chosen significance level, that suggests that the observed data is sufficiently inconsistent with the null hypothesis, and the null hypothesis may be rejected.

B. Skewness and Kurtosis Study

Skewness and kurtosis are usually used to check if I and Q components are Gaussian distributed [67]. The skewness, $\gamma_3 = E[(X-\mu_x)^3]/E[(X-\mu_x)^2]^{3/2}$, measures the degree of asymmetry of a PDF with respect to its mean μ_x, being zero for symmetric PDFs. In radar literature, the "excess kurtosis", $\gamma_{4,exc} = \gamma_4 - 3$, being $\gamma_4 = E[(X-\mu_x)^4]/E[(X-\mu_x)^2]^2$, is used to analyse the non-Gaussian nature of the data: negative $\gamma_{4,exc}$ are generated by PDFs with a rate of decay higher than the Gaussian PDF; positive $\gamma_{4,exc}$ are generated by higher tails, typical of impulsive signals [42].

V. Radar Scenario

The radar scenario is the same as that described in [48]. In Fig. 4, two Areas of Interest (AoI) were defined by the surveillance antenna beamwidth of 30° (in green), and 60° (in orange). Two potential IoOs were identified: Torrespaña, with an Equivalent Radiated Power, ERP, equal to 20 kW, and Algete, with an ERP equal to 11.8 W. The former was selected as the main IoO; Algete was discarded as interfering IoO because it was out of the orange AoI. In Fig. 5, the view from the surveillance antenna is shown. The targets to be sought were vehicles moving along the R2 highway (in light blue) and the Meco road (in dark blue). A parking area with trees and three Big Buildings (BBs) were identified: **BB1** (a research institute, made of Aluminium); **BB2** (textile industry); **BB3** (industrial area).

Speeds lower than 6.5 km/h in the R2 highway and the Meco road gave rise to Doppler shifts close to the zero Doppler line of the CAF, $-10 < f_d < 10$ Hz; but in a roundabout, targets speeds up to 35 km/h would generate Doppler shifts in this range, proving the impact of the radar system geometry in the

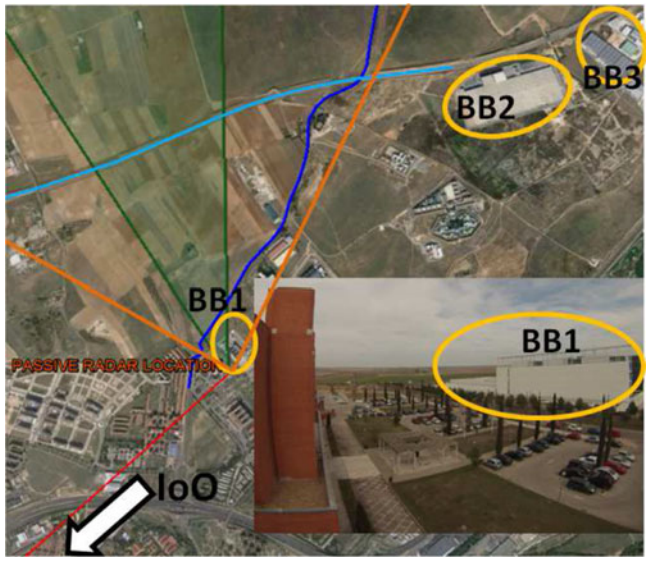

Fig. 5. View from the surveillance antenna.

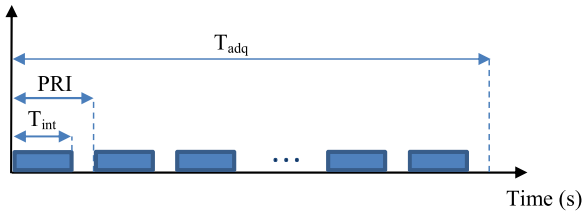

Fig. 6. Time processing parameters definition.

expected bistatic Doppler shifts. BBs were expected to reflect a strong signal, whose maximum values would be concentrated on the zero Doppler line of the CAF, at different bistatic range bins.

A. Observation Space Parameters

A database composed of acquisitions of $T_{acq} = 20$ s. was generated controlling that there wasn't any moving car in the scenario during system operation. Each acquisition was divided into Coherent Processing Intervals (CPIs) of duration T_{int} s., the integration time, using a periodic pulse train with a selected Pulse Repetition Interval (PRI) (Fig. 6).

PRI defines the data updating speed and is selected according to the implemented signal processing scheme and system application (as an example, in [54] $PRI = 0.6$ s and $T_{int} = 0.5$ s). In this work, $PRI = T_{int}$.

Taking into consideration desired targets dynamics, $PRI = T_{int} = 250$ ms was selected in [48]. In this work, $T_{int} \in \{250\,\text{ms}, 500\,\text{ms}\}$ were used, for evaluating the impact of system Doppler resolution in clutter characterization.

Each CAF matrix was composed of 1,000 range bins, covering a distance of 9.450 km along the pointing direction. Doppler ranged from −799.744 Hz to 799.744 Hz, but the frequency step depended on T_{int}: 4 Hz for $T_{int} = 250$ ms, and 2 Hz for $T_{int} = 500$ ms. Different Doppler regions were defined follow-

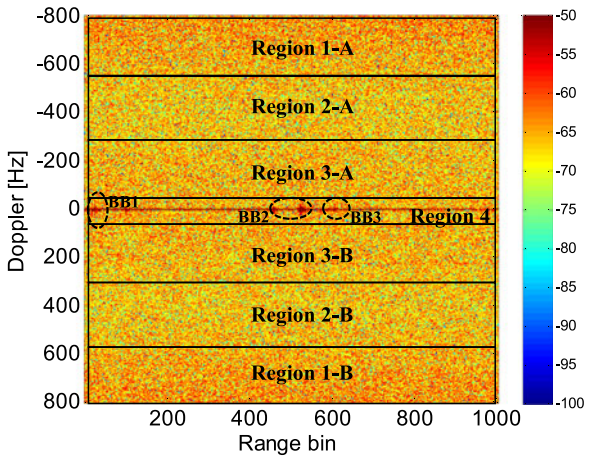

Fig. 7. Example of CAF function (normalized magnitude in dB), with the defined study regions and BBs contributions maxima.

ing a subjective criterion based on CAF magnitude mean level estimation, and possible targets Doppler shifts (Fig. 7):

- Areas far from the zero Doppler: 1A $[-799; -550]$ Hz, and 1B $[550; 799]$ Hz.
- Areas where aircrafts flying at low altitudes could be detected: 2A $(-550; -300]$ Hz, and 2 B $[300; 550)$ Hz.
- Areas where terrestrial vehicles are expected [48]: 3A $(-300; -40]$ Hz, 3B $[40; 300)$ Hz, and 4 $(-40; 40)$ Hz. Area 4 is of special interest because it concentrates ground clutter highest contributions.

For saving space, and without loss of generality nor accuracy, the data acquired on February 13, 2015 were selected. I and Q components were identically distributed, because of that, only the results related to the I component were included. The PDF of data amplitude can be obtained from the PDF of their intensity, so only intensity results are presented. For each clutter region, KS-Test2 and CM-Test2 goodness-of-fit tests (5% significance level), skewness, kurtosis, and Autocorrelation Functions (ACFs) were analysed.

VI. Statistical Analysis Results

In Table III, d_{KS}, d_{CM}, and p_{CM} values for regions 1, 2 and 3, $T_{int} = 250$ ms and 500 ms, are shown.

- Intensity was exponentially distributed. Weibull, Gamma and K-distributions also were accepted, with estimated parameters quite close to the values that make them equal to the exponential.
- The Log-normal distribution was discarded. d_{KS} and d_{CM} values belonged to $[0.068, 0.072]$ and $[47.90, 124]$, respectively, with $p_{CM} = 0$.
- The I component was Gaussian distributed. The study of the skewness and excess kurtosis values for I and Q components confirmed it.

Statistical parameters were similar in regions $i - A$ and $i - B$, and depended on T_{int}. Fig. 8 represent the standard deviations (std) of the I components for the different regions.

TABLE III
Goodness-of-Fit Test Distances and p-value for CM-Test2 With $\alpha = 0.05$; Regions $i - A$ and $i - B$, $i = 1, 2, 3$

	Intensity			Q component		
	E, $T_{int} = 250$ ms			N, $T_{int} = 250$ ms		
	d_{KS}	d_{CM}	p_{CM}	d_{KS}	d_{CM}	α_{CM}
1A	0.005	0.15	0.3738	0.008	1.15	0.2277
2A	0.004	0.07	0.7533	0.003	0.08	0.5186
3A	0.004	0.07	0.7522	0.005	0.54	0.5799
4	**0.92**	**3138**	**0**	**0.94**	**6341**	**0**
3B	0.004	0.08	0.7079	0.004	0.20	0.7857
2B	0.005	0.19	0.2950	0.003	0.08	0.2527
1B	0.008	0.55	0.3012	0.007	1.27	0.6362
	E, $T_{int} = 500$ ms			N, $T_{int} = 500$ ms		
1A	0.005	0.22	0.4321	0.003	0.09	0.6199
2A	0.005	0.114	0.7118	0.003	0.09	0.6314
3A	0.003	0.10	0.3730	0.002	0.04	0.9182
4	**0.42**	**682**	**0**	**0.42**	**1370**	**0**
3B	0.004	0.06	0.2623	0.002	0.082	0.6783
2B	0.005	0.21	0.6937	0.001	0.03	0.9809
1B	0.004	0.09	0.2930	0.003	0.23	0.2091

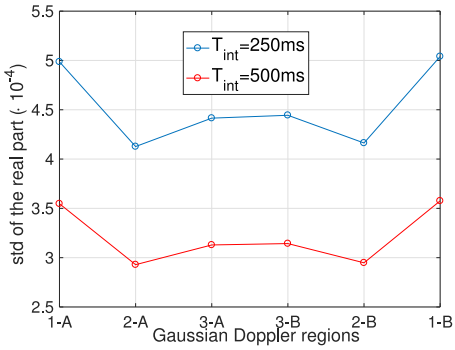

Fig. 8. Standard deviation (std) of the I component in the Gaussian regions of the CAF.

In region 4 all distributions were rejected (bold numbers in Tables III and IV). Q samples had negative skewness and positive excess kurtosis: $\gamma_3 = -2.342$ and $\gamma_{4,exc} = 469.957$ for $T_{int} = 250$ ms, and $\gamma_3 = -2.889$ and $\gamma_{4,exc} = 867.027$ for $T_{int} = 500$ ms; skewness and positive excess kurtosis values for I were quite different: $\gamma_3 = -19.740$ and $\gamma_{4,exc} = 1,776$ for $T_{int} = 250$ ms, and $\gamma_3 = -26.655$ and $\gamma_{4,exc} = 3,283$ for $T_{int} = 500$ ms.

A. Study of the Non-Gaussian Region of the CAF

Region 4 was divided into different sub-regions:

- $T_{int} = 250$ ms. Doppler resolution of 4 Hz.
  Intervals (Hz): $[-42, -18)$; $[18, 30)$; $[30, 42)$.
  Lines (Hz): $[-18, -14)$; $[-14, -10)$; $[-10, -6)$; $[-6, -2)$; $[-2, 2)$; $[2, 6)$; $[6, 10)$; $[10, 14)$; $[14, 18)$.
- $T_{int} = 500$ ms. Doppler resolution of 2 Hz.
  Intervals (Hz): $[-41, -15)$; $[-15, -9)$; $[15, 31)$; $[31, 41)$.
  Lines (Hz): $[-9, -7)$; $[-7, -5)$; $[-5, -3)$; $[-3, -1)$; $[-1, 1)$; $[1, 3)$; $[3, 5)$; $[5, 7)$; $[7, 9)$; $[9, 11)$; $[11, 13)$; $[13, 15)$.

TABLE IV
GOODNESS-OF-FIT TEST DISTANCES AND p-VALUE FOR CM-TEST2 WITH $\alpha = 0.05$; REGION 4; $T_{int} \in \{250\,\text{ms}, 500\,\text{ms}\}$

Intensity, $T_{int} = 250$ ms													Q component, $T_{int} = 250$ ms		
W			K			LN			Γ				LG		
d_{KS}	d_{CM}	p_{CM}	d_{KS}	d_{CM}	p_{CM}	d_{KS}	d_{CM}	p_{CM}	d_{KS}	d_{CM}	p_{CM}	d_{KS}	d_{CM}	p_{CM}
0.22	**210**	**0**	**0.96**	**3051**	**0**	**0.13**	**49**	**0**	**0.46**	**630**	**0**	**0.16**	**123**	**0**
Intensity, $T_{int} = 500$ ms													Q component, $T_{int} = 500$ ms		
0.20	**396**	**0**	**0.96**	**5913**	**0**	**0.11**	**68**	**0**	**0.48**	**1313**	**0**	**0.08**	**46**	**0**

TABLE V
GOODNESS-OF-FIT TESTS FOR REGION 4; $T_{int} = 250$ MS AND $T_{int} = 500$ MS

f_d (Hz)	Intensity, $T_{int} = 250$ms			Real part, $T_{int} = 250$ms			Intensity, $T_{int} = 500$ms			Real Part, $T_{int} = 500$ms		
	PDF	d_{CM}	p_{CM}	PDF	d_{CM}	p_{CM}	PDF	d_{CM}	p_{CM}	PDF	d_{CM}	p_{CM}
$[-15,-14)$	E	0.114	0.5221	N	0.113	0.5255	E	0.17	0.3216	N	0.08	0.7126
$[-14,-13)$ $[-13,-12)$ $[-12,-11)$ $[-11,-10)$	$2-\Gamma MD$	0.06	0.8197	$2-GMD$	0.096	0.6810	2-ΓMD	0.06	0.8216	$2-GMD$	0.12	0.5066
$[-10;-9)$ $[-9;-8)$ $[-8;-7)$ $[-7;-6)$	$2-\Gamma MD$	0.09	0.6496	$2-GMD$	0.09	0.6148	2-ΓMD	0.13	0.4371	$2-GMD$	0.05	0.8441
$[-6;-5)$							$2-\Gamma MD$	0.02	0.9914	$2-GMD$	0.14	0.9032
$[-5;-4)$ $[-4;-3)$ $[-3;-2)$	$2-\Gamma MD$	0.16	0.3687	$2-GMD$	0.15	0.3759	$2-\Gamma MD$	0.12	0.5082	$2-GMD$	0.04	0.5746
$[-2;-1)$							$2-\Gamma MD$	0.11	0.5412	$2-GMD$	0.11	0.5246
$[-1;0)$ $[0;1)$ $[1;2)$	**LN**	**8.66**	**1**	$4-MGD$	0.33	0.11	**LN**	**3.99**	**1**	$4-GMD$	0.21	0.6540
							$2-\Gamma MD$	0.05	0.8646	$2-GMD$	0.37	0.088

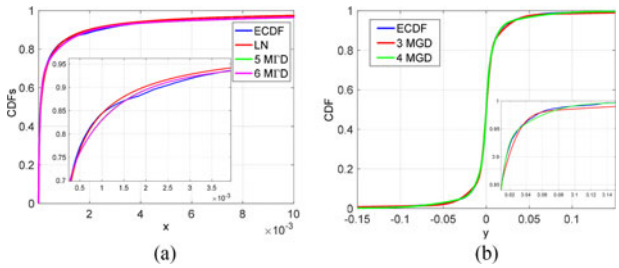

Fig. 9. CDFs for the zero Doppler line and $T_{int} = 250$ ms. (a) Intensity. (b) Real part.

Table V presents the accepted distributions and the associated d_{CM} and p_{CM} values. Subregions far away from the zero Doppler line are Gaussian distributed. Weibull, K and Gamma distributions were also accepted for the intensity, with estimated parameters that made them equal to the Exponential. The I component can be modeled with $4-GMDs$ along the zero Doppler, but any of the considered intensity distributions passed the tests. Fig. 9 shows the ECDFs and some estimated ones for the zero Doppler line and $T_{int} = 250$ ms.

Fig. 9(a) presents the LN CDF, together with the estimated 5 and $6-\Gamma MDs$. Fig. 9(b) depicts CDFs for the 4 and $3-GMDs$ to show the error associated to the latest. Data obtained with $T_{int} = 250$ ms were used; results were similar for $T_{int} = 500$ ms. For the rest of Doppler subregions, $2-\Gamma MD$ and $2-GMD$ are proposed for the intensity and the I component, respectively. In Fig. 10, ECDFs are compared to the theoretical models for two Doppler lines: that associated to the lowest Doppler shifts for region 4, and that just next to the zero Doppler.

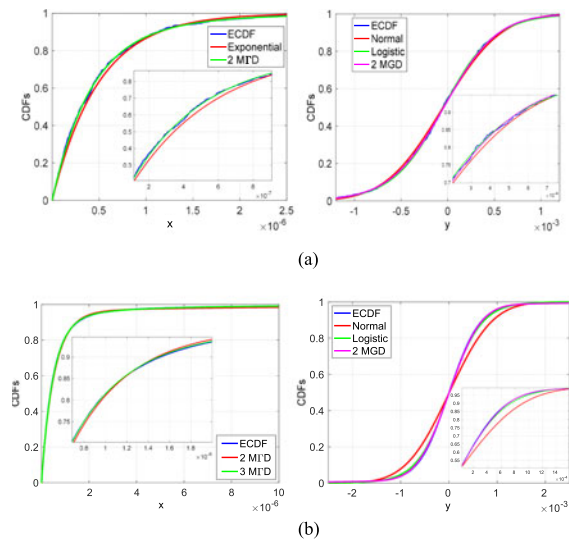

Fig. 10. CDFs for region 4 and $T_{int} = 250$ ms: $f_d \in [-14,-10)$Hz (top); $f_d \in [-6,-2)$Hz (bottom). (a) Intensity (left), I component (right), $[-14,-10)$ Hz. (b) Intensity (left), I component (right), $[-6,-2)$ Hz.

The Exponential distribution is depicted in the first case (left image in Fig. 10) to show the difference with respect to the empirical one; in the second case, $2-\Gamma MD$ and $3-\Gamma MD$ are

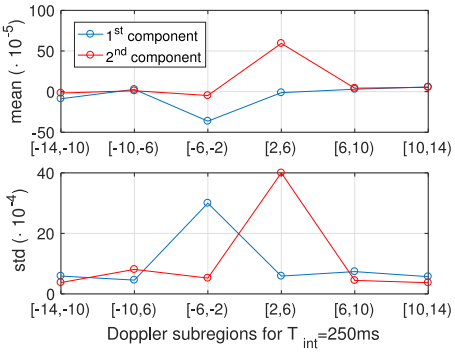

Fig. 11. $2-GMDs$ parameters for the I component and $T_{int}=250$ ms.

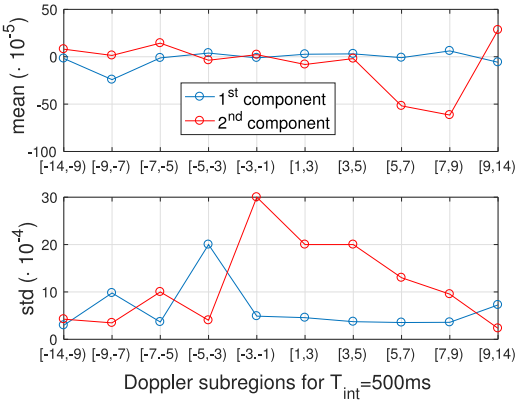

Fig. 12. $2-GMDs$ parameters for the I component and $T_{int}=500$ ms.

TABLE VI
PARAMETERS OF THE $4-MGD$ IN $[-2,2)$ HZ FOR $T_{int}=250$ MS

Component	$1st$	$2nd$	$3rd$	$4th$
$\mu\cdot 10^{-2}$	11.80	0.1922	0.0640	-0.02680
Std $\cdot 10^{-2}$	35.60	5.33	1.20	0.3280

plotted to show that although $3-\Gamma MD$ could have been chosen by visual inspection, the $2-\Gamma MD$ passed the test and was selected due to its simplicity. Figs. 11 and 12 show the variation of the $2-GMD$ parameters throughout the defined Doppler subregions for $T_{int}=250$ ms and $T_{int}=500$ ms, respectively. $4-MGD$ parameters for Doppler region $[-2,2)$Hz and $T_{int}=250$ ms are included in Table VI.

VII. LR DETECTOR FORMULATION

For the formulation of the NP detector, the likelihood functions of the complex observation vector are required (expression (1)). In the case of study, this vector is composed of a single complex sample, $\bar{\mathbf{z}}=\widetilde{z}$, so the joint pdf of $\bar{\mathbf{z}}=[Re\{\widetilde{z}\},Im\{\widetilde{z}\}]^T=[z_1,z_2]^T$ under both hypotheses must be estimated (T denotes the transpose operation). Although the detectors are applied to a single complex sample, the CFAR techniques required for estimating the detection thresholds will process the data in range reference windows. Because of that, joint PDFs and Autocorrelation Functions (ACFs) along range are analysed in the

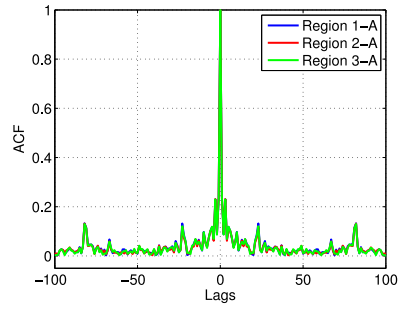

Fig. 13. Estimated normalized ACF along range for $T_{int}=250$ ms, and regions $i-A$, $i=1,2,3$.

TABLE VII
ESTIMATED P_{FA} FOR CA-CFAR DETECTORS WITH DIFFERENT ρ: REGIONS 1–3, DESIRED $P_{FA}=10^{-4}$

N_r	$\rho=0$	$\rho=0.2322$
16	$7.1612\cdot 10^{-5}$	$8.705\cdot 10^{-5}$
32	$8.684\cdot 10^{-5}$	$9.613\cdot 10^{-5}$
64	$8.937\cdot 10^{-5}$	$9.549\cdot 10^{-5}$
100	$9.402\cdot 10^{-5}$	$9.719\cdot 10^{-5}$

following subsections. For saving space, from now on, only results for $T_{int}=250$ ms will be included. Conclusions were similar for $T_{int}=500$ ms with different sets of parameters.

A. Gaussian Areas of the CAF

As I and Q components are Gaussians, they are independent, and the likelihood function of $\bar{\mathbf{z}}$ can be expressed as the product of its marginals. A possible implementation of the NP detector consists in comparing $|\bar{\mathbf{z}}|^2$ with a detection threshold selected according to P_{FA} requirements [52].

The basic Cell-Averaging CA-CFAR detector is optimum when input samples are independent and identical distributed exponential random variables. To check the suitability of this CFAR technique, the ACFs along range were estimated for regions $i-A$, $i=1,2,3$ (Fig. 13). Similar results were obtained for regions $i-B$, $i=1,2,3$. The estimated average one-lag correlation coefficient was $\rho_{range}=0.2322$.

The ACFs presented peaks, lower than 0.2 except for the samples close to the main peak. To evaluate their impact on the detection process, CA-CFAR detectors were implemented for $\rho_{range}=0$ and $\rho_{range}=0.2322$, and applied to the squared magnitude of the complex data, using N_r-length range reference windows [68]. This simple methodology is based on the hypothesis that if the estimated ρ_{range} was relevant, the CA-CFAR designed for $\rho_{range}=0.2322$ would present better performance than the CA-CFAR designed for $\rho_{range}=0$. The estimated P_{FA} was used as performance parameter. In Table VII the estimated P_{FAs} are very similar and close to the desired one, so we could conclude that the impact of the correlation peaks on the detection performance was negligible, and in regions $i-A$ and $i-B$, $i=1,2,3$, CAF samples could be assumed to be uncorrelated along range.

TABLE VIII
ESTIMATED PARAMETERS FOR THE MIXTURES OF 2-D GAUSSIANS

Doppler	k_1	$10^{-4}\cdot\mu_1$	$10^{-6}\cdot\mathbf{C}_1$	k_2	$10^{-4}\cdot\mu_2$	$10^{-6}\cdot\mathbf{C}_2$	d_{KS}	p_{KS}
$[-14,-10)$	0.6873	$[-0.264, 0.179]$	$\begin{bmatrix} 0.1665 & -0.0186 \\ -0.0186 & 0.1924 \end{bmatrix}$	0.3127	$[-1.048, -0.817]$	$\begin{bmatrix} 0.3994 & 0.0610 \\ 0.0610 & 0.3816 \end{bmatrix}$	0.0530	0.2
$[-10,-6)$	0.0175	$[-1.0044, -0.5305]$	$\begin{bmatrix} 2.319 & 0.108 \\ 0.108 & 2.204 \end{bmatrix}$	0.9825	$[0.2665, -0.5305]$	$\begin{bmatrix} 0.2533 & -0.0023 \\ -0.0023 & 0.2497 \end{bmatrix}$	0.0430	0.2
$[-6,-2)$	0.9314	$[-0.494, -0.019]$	$\begin{bmatrix} 0.256 & -0.002 \\ -0.002 & 0.275 \end{bmatrix}$	0.0686	$[-1.881, -3.288]$	$\begin{bmatrix} 3.253 & -0.073 \\ -0.073 & 3.427 \end{bmatrix}$	0.0490	0.2
$[2,6)$	0.0772	$[2.999, 0.175]$	$\begin{bmatrix} 8.674 & -2.429 \\ -2.429 & 6.417 \end{bmatrix}$	0.9228	$[-0.089, -0.723]$	$\begin{bmatrix} 0.326 & -0.003 \\ -0.003 & 0.305 \end{bmatrix}$	0.0540	0.2
$[6,10)$	0.0606	$[-0.587, .0.166]$	$\begin{bmatrix} 0.970 & -0.071 \\ -0.071 & 1.303 \end{bmatrix}$	0.9394	$[0.459, -2.975]$	$\begin{bmatrix} 0.233 & 0.006 \\ 0.006 & 0.220 \end{bmatrix}$	0.0520	0.2
$[10,14)$	0.9868	$[0.555, 0.627]$	$\begin{bmatrix} 0.238 & 0.006 \\ 0.006 & 0.233 \end{bmatrix}$	0.0132	$[0.6255.967]$	$\begin{bmatrix} 0.255 & -0.500 \\ -0.500 & 1.663 \end{bmatrix}$	0.0540	0.2
$[14,18)$	0.0169	$[0.304, -1.476]$	$\begin{bmatrix} 1.470 & 1.379 \\ 1.379 & 2.486 \end{bmatrix}$	0.9831	$[-0.654, 0.266]$	$\begin{bmatrix} 0.222 & -0.010 \\ -0.010 & 0.202 \end{bmatrix}$	0.0420	0.2
$[18,30)$	0.4246	$[0.372, -0.236]$	$\begin{bmatrix} 0.292 & 0.046 \\ 0.046 & 0.185 \end{bmatrix}$	0.5754	$[-0.104, 0.283]$	$\begin{bmatrix} 0.189 & -0.031 \\ -0.031 & 0.249 \end{bmatrix}$	0.0343	0.2

Doppler intervals defined for $T_{int} = 250$ ms.
$i = 1, 2, 3, 4$ stand for the considered component of the 4-MGD.

TABLE IX
ESTIMATED PARAMETERS FOR THE $4-MGD$ PROPOSED FOR THE DOPPLER INTERVAL $[-2, 2)$ HZ AND $T_{int} = 250$ ms

k_i	$10^{-4}\cdot\mu_i$	$10^{-6}\cdot\mathbf{C}_i$
0.4132	$[-1.005, 1.034]$	$\begin{bmatrix} 13.6 & -1 \\ -1 & 10.3 \end{bmatrix}$
0.1684	$[2, 9.509]$	$\begin{bmatrix} 2,396 & 148 \\ 148 & 2,487 \end{bmatrix}$
0.0112	$[646, -1, 410]$	$\begin{bmatrix} 94\cdot10^3 & -27\cdot10^3 \\ -27\cdot10^3 & 39\cdot10^3 \end{bmatrix}$
0.4072	$[8.289, -2.871]$	$\begin{bmatrix} 139 & -12 \\ -12 & 143 \end{bmatrix}$
$d_{KS} = 0.038, p_{KS} = 0.2$		

B. Non-Gaussian Areas of the CAF

I and Q components were orthogonal, but, as they weren't Gaussian, we couldn't assume they were independent. The Expectation-Maximization (EM) algorithm was used for estimating their joint distributions as mixtures of 2D Gaussians (3), [69]. The complete region was studied due to its asymmetry with respect to the zero Doppler. $N = 2$ for all subregions except for the zero Doppler, which required $N = 4$; $\bar{\mu}_i$ and $\mathbf{C}_i$ are the mean vector and the covariance matrix of the $i-th$ component, respectively; $|\mathbf{C}_i|$ denotes the determinant of $\mathbf{C}_i$, and k_i are the mixture coefficients, $(k_1 + \cdots + k_N = 1)$.

$$f(\bar{\mathbf{z}}) = \sum_{i=1}^{N} \frac{k_i}{2\pi\cdot\sqrt{|\mathbf{C}_i|}} \cdot \exp\left(\frac{-(\bar{\mathbf{z}}-\bar{\mu}_i)^T\cdot\mathbf{C}_i^{-1}\cdot(\bar{\mathbf{z}}-\bar{\mu}_i)}{2}\right) \tag{3}$$

Tables VIII and IX summarize the estimated parameters, and the results of the 2D-KS-test2 algorithm [70], proving that the proposed distributions fulfilled the test. Results of the correlation study showed again peaks lower than 0.2, except for the samples close to the main peak, whose impact in detection performance was neglected (Fig. 14).

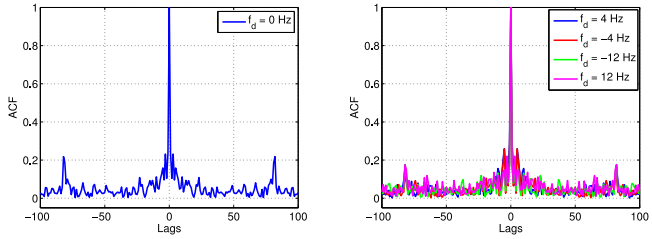

Fig. 14. Estimated normalized ACFs along range for $T_{int} = 250$ ms.

For obtaining $f(\bar{\mathbf{z}}|H_1)$, a Gaussian target model was assumed (Gaussians I and Q components of zero mean and variance σ^2_{target}). The total mean vector of $f(\bar{\mathbf{z}}|H_0)$ was calculated as $\bar{\mu}_{total} = \sum_{i=1}^{N} k_i\cdot\bar{\mu}_i$; the total covariance matrix was calculated as $\mathbf{C}_{total} = \sum_{i=1}^{N} k_i(\mathbf{C}_i + (\bar{\mu}_i - \bar{\mu}_{total})\cdot(\bar{\mu}_i - \bar{\mu}_{total})^T)$, with $N = 2$ for all subregions except the one centred on the zero Doppler, for which $N = 4$.

For generating samples of $f(\bar{\mathbf{z}}|H_0)$, samples of the individual components must be generated with probabilities equal to the mixture coefficients. When a target is present, its covariance matrix ($\mathbf{C}_{target} = \sigma^2_{target}\cdot\mathbf{I}$, being $\mathbf{I}$ the 2D identity matrix) is added to the covariance matrixes of the individual components of the H_0 mixture, to obtain $f(\bar{\mathbf{z}}|H_1)$. The Signal-to-Interference Ratio (SIR) is defined as $SIR = 10\log_{10}(\frac{2\sigma^2_{target}}{tr(\mathbf{C}_{total})})$, where $tr(\mathbf{C}_{total})$ denotes the trace of $\mathbf{C}_{total}$. The LR detector is expressed in (4).

$$\frac{\sum_{i=1}^{N} \frac{k_i \exp\left(\frac{-(\bar{\mathbf{z}}-\bar{\mu}_i)^T\cdot(\mathbf{C}_i+\sigma^2_{target}\mathbf{I})^{-1}\cdot(\bar{\mathbf{z}}-\bar{\mu}_i)}{2}\right)}{2\pi\cdot\sqrt{|\mathbf{C}_i+\sigma^2_{target}\mathbf{I})|}}}{\sum_{i=1}^{N} \frac{k_i \exp\left(\frac{-(\bar{\mathbf{z}}-\bar{\mu}_i)^T\cdot\mathbf{C}_i^{-1}\cdot(\bar{\mathbf{z}}-\bar{\mu}_i)}{2}\right)}{2\pi\cdot\sqrt{|\mathbf{C}_i|}}} \underset{H_0}{\overset{H_1}{\gtrless}} \eta_{lr}(P_{FA}) \tag{4}$$

The SIR value associated to the σ^2_{target} used in expression (4) will be denoted as SIR_d; while the SIR value associated

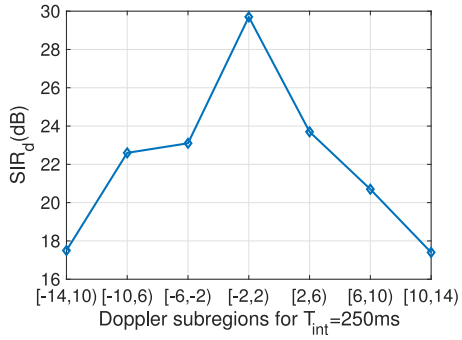

Fig. 15. SIR_d for the design of the LR detectors for $T_{int} = 250$ ms.

to the σ^2_{target} used for generating synthetic data as input of (4) to estimate P_D will be denoted as SIR_s. P_D was estimated for $SIR_d = SIR_s$, to determine the minimum SIR_d values for $P_D \geqslant 80\%$, and $P_{FA} = 10^{-4}$ for the different subregions (Fig. 15). These SIR_d values will be used for implementing the bank of LR detectors (4).

Results presented in Fig. 15 were generated following this methodology:

1) Vectors of 10^6 complex samples under H_0 were generated with the parameters included in Fig. 8, and Tables VIII and IX. As the parameters of regions $i - A$ and $i - B, i = 1, 2, 3$, were similar, a total of 12 vectors were generated: 9 for region 4, and 3 for the Gaussian areas.
2) For each region, LR detectors were built for SIR_d ranging from 10 dB to 40 dB in steps of 0.1 dB. Detection thresholds for $P_{FA} = 10^{-4}$ were estimated for each LR by Monte Carlo simulations using the data sets described in the previous step (estimation error lower than 10%).
3) 12 vector sets were generated under H_1 for P_D estimation: one set for each CAF region. Each set was composed of vectors of 1000 samples: one vector for each SIR_s ranging from 10 dB to 40 dB in steps of 0.1 dB.
4) The set of H_1 vectors designed for a region was applied to the LR detectors of that region designed for $SIR_s = SIR_d$ varying from 10 dB to 40 dB in steps of 0.1 dB. P_D was estimated by Monte Carlo simulations using the detection thresholds estimated in step 2.

The outputs of three detection schemes for a CPI are presented in Fig. 16: (a) a square-law envelope detector applied to the CAF output; (b) a zero Doppler suppression technique based on an Extensive CAncellation (ECA) filter, the CAF, and an square-law envelope detector [48]; (c) bank of LR detectors applied to the CAF. Results prove the better performance of the bank of LR detectors in clutter suppression.

VIII. MLP-CFAR for the Bank of LR Detectors

The complexity of expression (4), the variability of SIR_d, k_i, $\bar{\mu}_i$, and $\mathbf{C}_i$, $i = 1, ..., N$, along Doppler, and the computational cost associated to P_{FA} estimations, motivate the proposal of an alternative CFAR technique to be applied to Fig. 16(c). Taking [49] as a starting point, the objective was the design of a single MultiLayer Perceptron (MLP) with one hidden layer capable of estimating the desired detection thresholds. The proposed solution is presented in Fig. 17: a sliding range window of $2(R + R_{guard} + 1)$ cells is shifted along each Doppler line of the output of the bank of LR detectors ($2R$ reference cells for estimating the detection threshold, $2R_{guard}$ cells for avoiding the contribution of target components when a target is in the cell under test (CUT), and the CUT); Doppler lines are processed sequentially, reference cells are applied to the MLP-CFAR, which will generate a threshold for the associated CUT.

For training the MLP, independent synthetic data sets were generated for training, cross-validation and testing. Each set was composed of $R - length$ vectors generated under H_0, with the parameters included in Fig. 8, and Tables VIII and IX. After a study of the scenario and targets dynamics, $R = 32$ and $R_{guard} = 6$ were selected. The training set was composed of 9, 000 patterns, 750 patterns per clutter region ($i - A, i = 1...3$, and the 9 subregions defined in region 4 for $T_{int} = 250$ ms). Validation and test sets had the same structure, with 250 and 10^6 patterns per clutter subregion, respectively. The detection thresholds estimated for the implemented LR detectors bank, for a $P_{FA} = 10^{-4}$, were used as desired outputs.

The Levenberg-Marquardt optimization algorithm was applied for MLP training. This algorithm uses the sum of squares error as objective function and an approximation of the Hessian matrix based on the Jacobian matrix in a Newton based updating rule [71]. If $\bar{\mathbf{w}} = [w_1, ..., w_P]$ is the vector composed of all the MLP weights and bias, the updating rule in iteration n is $\bar{\mathbf{w}}(n+1) = \bar{\mathbf{w}}(n) - \left(\mathbf{J}^T(n) \cdot \mathbf{J}^T(n) + \mu \mathbf{I}\right)^{-1} \cdot \mathbf{J}^T(n) \cdot e(\bar{\mathbf{w}}(n))$, where:

- $e(\bar{\mathbf{w}}(n)) = \frac{1}{2} \sum_{j=1}^{N_{train}} e^2(j)$ is the error, being N_{train} the number of training patterns and $e(i)$ the difference between the MLP output and the desired one for the $i - th$ pattern of the training set, in the $n - th$ iteration.
- $\mathbf{J}(n)$ is the Jacobian matrix of $e(\bar{\mathbf{w}}(n))$. It's a N_{train}xP matrix and the element in row i and column j is calculated as $\mathbf{J}[i, j] = \frac{\partial e(i)}{\partial w_j}$.
- μ is a positive constant that is chosen to guarantee that the matrix to be inverted is definite positive. If $\mu = 0$ the updating rule is equal to the Newton's method one; if μ is high, the rule algorithm behaves as a gradient descent one with a small step size. The aim is to shift toward Newton's method as quickly as possible. Thus, μ is decreased after each successful step, and it is increased when a tentative step would increase the performance function.

For determining the number of hidden neurons, M, MLPs with $M \in \{3, 4, 5, 7\}$ were trained, following a methodology based on NN growing [72]. Fig. 18 shows the detection thresholds estimated by each MLP, for the Doppler regions defined for $T_{int} = 250$ ms, and a desired $P_{FA} = 10^{-4}$. The minimum estimated mean squared error between the desired and the estimated thresholds was obtained for $M = 4$. Because of that, $M = 4$ was elected.

For detection performance evaluation, the time parameters used in [48] were selected: $T_{acq} = 30$ s, $T_{int} = PRI = 250$ ms. Fig. 19 shows the superposition of detectors outputs for the 120 CPIs of an acquisition.

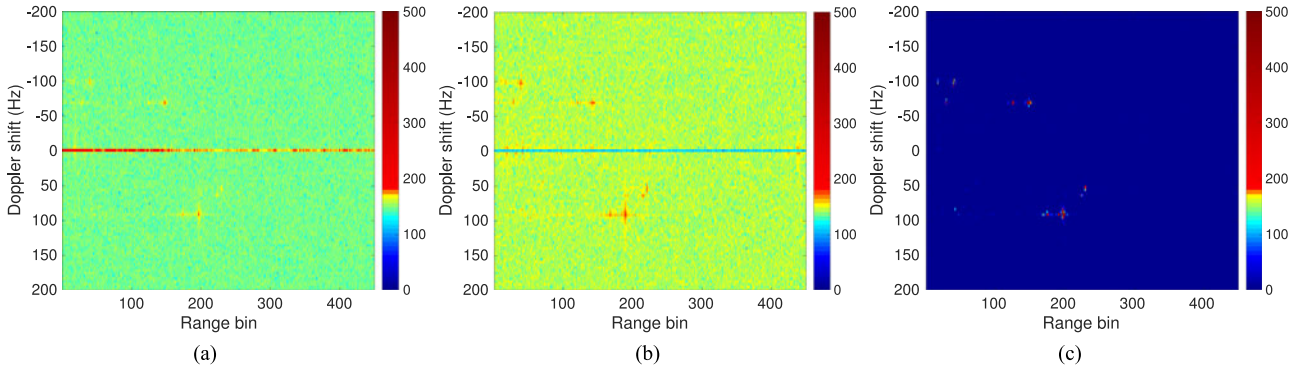

Fig. 16. Amplitude (dB) of the outputs generated by a square-law envelope detector applied to the CAF output (a). ECA filter, CAF, and an square-law envelope detector (b). Bank of LR detectors applied to the CAF (c).

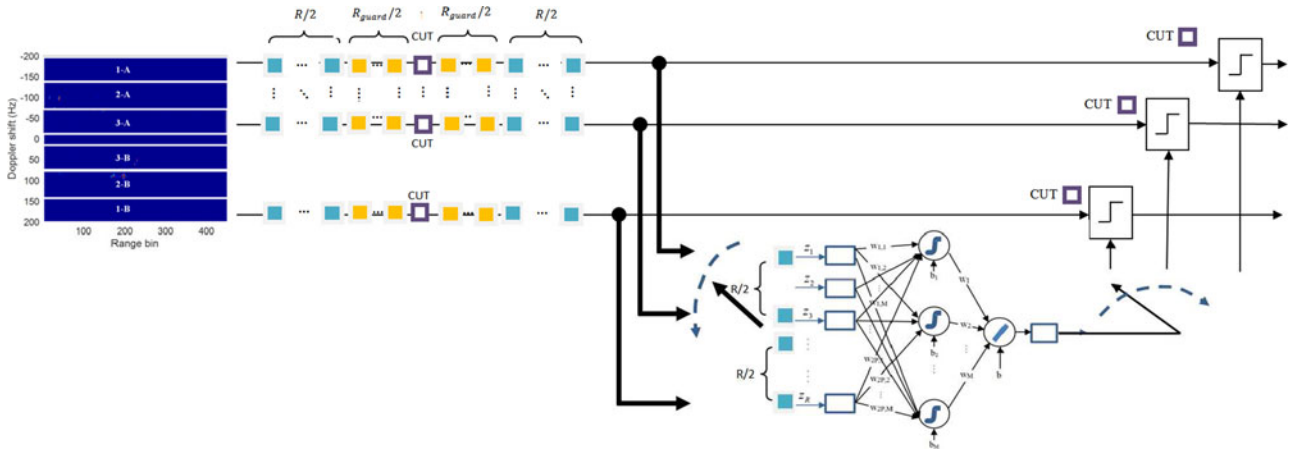

Fig. 17. Proposed MLP-CFAR scheme.

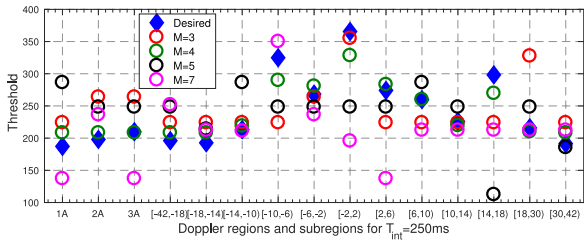

Fig. 18. Detection thresholds estimated by MLPs with different number of hidden neurons for a desired $P_{FA} = 10^{-4}$.

P_{FA} was estimated by Monte Carlo simulations for the whole CAF and Region 4:

1) Whole CAF: $\widehat{P}_{FA} = 3.23 \cdot 10^{-4}$ for the CA-CFAR; $\widehat{P}_{FA} = 1.85 \cdot 10^{-4}$ for the bank of LR detectors and the MLP-CFAR trained for $P_{FA} = 10^{-4}$. Estimation error: 1.8%.
2) Region 4: $\widehat{P}_{FA} = 3.2 \cdot 10^{-3}$ for the CA-CFAR; $\widehat{P}_{FA} = 6.97 \cdot 10^{-4}$ for the bank of LR detectors and the MLP-CFAR trained for $P_{FA} = 10^{-4}$. Estimation error: 7.71%.

$P_{FA}s$ estimated for both detection schemes using the whole CAF are higher than the desired one. The values estimated for the LR bank and the MLP-CFAR are closer to the desired ones. Most of the Doppler regions of the CAF were Gaussian distributed, because of that, P_{FA} was also estimated in Region 4, where non-Gaussian models concentrate. In this case, the LR bank with a MLP-CFAR clearly outperforms the CA-CFAR, as expected, but the estimated P_{FA} is significantly far from the desired one. This phenomenon was also observed in [49]: CA-CFAR detection threshold estimation rule is designed for the available set of R samples, and an estimation error is expected that will give rise to an overestimation of the detection threshold that guarantees the required P_{FA} at the expense of a loss in P_D (CFAR losses); the MLP-CFAR was trained to approximate the detection thresholds required by the LR detectors for infinite homogeneous regions, so the associated CFAR losses will be higher. To reduce them, a lower training P_{FA} value was estimated for determining the desired outputs (thresholds) to be estimated by the MLP [49]. Table X summarizes the considered training P_{FA} values and the estimated $P_{FA}s$ for the whole CAF and Region 4. Finally, the MLP trained for a desired $P_{FA} = 10^{-5}$ was selected, and the superposition of this detector outputs for an acquisition are shown in Fig. 20.

In [48], an ECA filter was applied before the CAF, to reduce zero Doppler interference; for a desired $P_{FA} = 10^{-6}$, the best detection scheme among those considered provided an estimated $\widehat{P}_{FA} = 5.499 \cdot 10^{-6}$, which means a relative error of 44.99%.

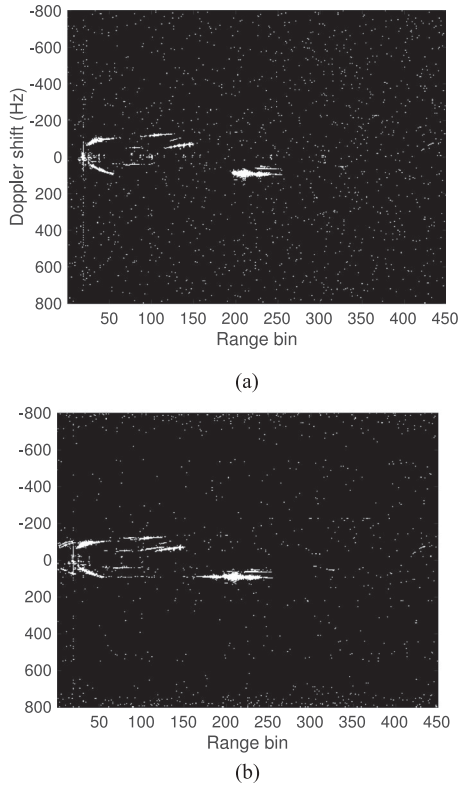

Fig. 19. Superposition of detectors outputs for an acquisition, and a desired $P_{FA} = 10^{-4}$. (a) Conventional CA-CFAR applied to Fig. 16(a). (b) MLP-CFAR with $M = 4$, trained with thresholds estimated for $P_{FA} = 10^{-4}$, applied to Fig. 16(c).

TABLE X
$\widehat{P}_{FA}$S FOR MLPS TRAINED FOR DIFFERENT P_{FA}S

Training P_{FA}	Whole CAF estimated P_{FA}	Region 4 estimated P_{FA}
10^{-4}	$1.85 \cdot 10^{-4}$	$6.97 \cdot 10^{-4}$
$7 \cdot 10^{-5}$	$1.84 \cdot 10^{-4}$	$6.96 \cdot 10^{-4}$
$5 \cdot 10^{-5}$	$1.56 \cdot 10^{-4}$	$6.042 \cdot 10^{-4}$
10^{-5}	$1.01 \cdot 10^{-4}$	$4.45 \cdot 10^{-4}$

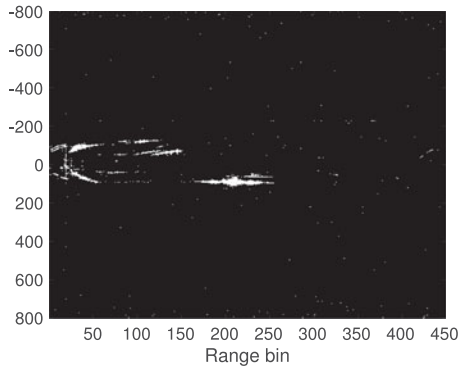

Fig. 20. Superposition of the outputs generated by the MLP-CFAR trained with thresholds estimated for $P_{FA} = 10^{-5}$, applied to Fig. 16(c).

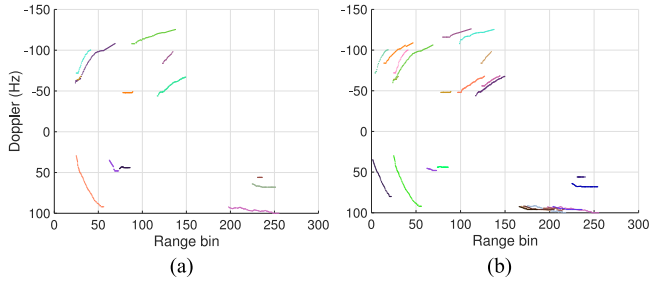

Fig. 21. Tracker outputs for the CA-CFAR (a), and the bank of LR detectors with the MLP-CFAR (b), for a desired $P_{FA} = 10^{-4}$.

Visual inspection of Fig. 20 demonstrates the superior performance of the MLP-CFAR trained for a desired $P_{FA} = 10^{-5}$. Results generated by the tracking system described in [48] are presented in Fig. 21. The LR detectors bank and the MLP-CFAR trained for $P_{FA} = 10^{-5}$ allowed the tracker to confirm a total of 25 tracks (also confirmed by visual information about non-cooperative targets), whereas from the CA-CFAR output only 13 tracks were confirmed. Considering the total length of the 25 tracks as a reference (a total of 1,031 points), detection performance was characterized as the number of plots generated after the detection stage divided by 1,031: 51% for the CA-CFAR, and 79% for the bank of LR detectors and the MLP-CFAR.

IX. CONCLUSION

In this paper, statistical and machine learning signal processing methods are combined as a step towards the automation of cognitive functionality in passive radars. In cognitive radars, the feedback from the receiver to the transmitter is a facilitator of intelligence; in passive radars, this feedback is not possible, but an intelligent algorithm capable of selecting the most suitable IoO among those available in the radar scenario can be designed and implemented. In any case, the capability of radar scenario characterization is a key element, being clutter of critical relevance. Because of that, a detailed study of statistical analysis tools and their application to real data acquired by an operating PR demonstrator is the first task to be tackled. One of the objectives of this paper is to demonstrate that the knowledge about the statistical characterization of the radar returns can be used to design machine learning based detectors, exploiting the concept of cognition in passive radars.

The considered case study was the use of a DVB-T based passive radar for terrestrial traffic monitoring in a semi-urban scenario. To approximate the Neyman-Pearson detector, a solution based on the LR detector was proposed, considering the following hypotheses:

1) Ground clutter can be characterized from measurements to model the likelihood function under H_0.
2) Ground clutter models are expected to present small variations along time, and these variations can be characterized to modify the proposed likelihood function under H_0.
3) A Gaussian target is assumed.

4) The proposed detector uses a single observation, but the associated CFAR technique uses a set of observations to estimate the detection threshold.
5) The detection rule discriminant function is expected to be complex. The capabilities of machine learning techniques will be exploited for designing a coherent CFAR technique for the proposed detection scheme.

To accomplish ground clutter characterization, real data acquired by the technological demonstrator IDEPAR, a multichannel DVB-T based PR demonstrator, were analyzed. The selected scenario was located at University of Alcalá external campus, a semi-urban environment characterized by the presence of big buildings, that were expected to generate strong radar returns, and parking areas. As Doppler resolution is a function of the integration time, two values were considered for comparison purposes.

To model the likelihood function under H_0, an exhaustive statistical analysis was performed throughout all the CAF space, without applying any pre-processing stage that could alter clutter statistics. ECDF estimations, goodness-of-fit tests, skewness and kurtosis, and correlation properties were analyzed to determine the most suitable clutter model among a representative selection of models proposed in the literature. Results proved that a Gaussian clutter model could be assumed for absolute Doppler shifts higher than 40 Hz. In the region centred in the zero-Doppler, with absolute value of Doppler shifts lower than 40 Hz, a non-homogeneous characterization was required. Mixtures of Γs and Gaussians were proposed for the intensity and the real (imaginary) parts, respectively. Two mixture components were enough in all cases, but for the zero Doppler line, where four mixture components were required.

For formulating the LR detector, the complex samples were characterized and mixtures of 2D-Gaussians were estimated. The correlation properties were also analysed, taking into consideration the operation principle of CFAR techniques. Results proved that CAF samples were uncorrelated along range, making the CA-CFAR detector the optimum solution for the Gaussian regions (the most part of the CAF).

A bank of LR detectors was implemented for the non-Gaussian region. Their output magnitude was compared with the output magnitude of the CAF and the combination of an ECA filter and the CAF, demonstrating the superior performance of the bank of LR detectors for clutter rejection.

Finally, the CFAR technique based on a MultiLayer Perceptron (MLP) proposed in [49] was generalized for designing a single neural network for estimating the detection thresholds to be applied to the output of the bank of LR detectors. A single MLP with 64 inputs, one hidden layer with four neurons, and one output is able to provide the required thresholds for guaranteeing the desired P_{FA} throughout all the CAF.

Presented results are expected to provide a deeper knowledge about the impact of ground clutter components on the detection of low Doppler shift targets. The proposed bank of LR detectors based on Gaussians mixtures is quite easy to implement and adapt to potential clutter changes. The MLP-CFAR can be easily retrained thanks to its simplicity and the possibility of generating synthetic data. On the other hand, the proposed solution could be used as a reference in future designs.

REFERENCES

[1] *IEEE Standard Radar Definitions*, IEEE Aerospace and Electronics System Society Sponsored by the Radar System Panel, ANSI/IEEE 686-2008, 2008.

[2] P. E. Howland, D. Maksimiuk, and G. Reitsma, "FM radio based bistatic radar," *IEE Proc.—Radar, Sonar Navigat.*, vol. 152, no. 3, pp. 107–115, Jun. 2005.

[3] H. D. Griffiths and N. R. W. Long, "Television-based bistatic radar," *IEE Proc. F Commun. Radar Signal Process.*, vol. 133, no. 7, pp. 649–657, Dec. 1986.

[4] M. Cherniakov *et al.*, "Experiences gained during the development of a passive BSAR with GNSS transmitters of opportunity," *Int. J. Navigat. Observ.*, vol. 2008, 2008, Art. no. 807958.

[5] M. Malanowski, K. Kulpa, and K. E. Olsen, "Extending the integration time in DVB-T-based passive radar," in *Proc. 8th Eur. Radar Conf.*, Oct. 2011, pp. 190–193.

[6] J. E. Palmer, H. A. Harms, S. J. Searle, and L. Davis, "DVB-T passive radar signal processing," *IEEE Trans. Signal Process.*, vol. 61, no. 8, pp. 2116–2126, Apr. 2013.

[7] D. Langellotti, F. Colone, P. Lombardo, and M. Sedehi, "DVB-T based passive bistatic radar for maritime surveillance," in *Proc. IEEE Radar Conf.*, 2014, pp. 1197–1202.

[8] M. Conti, D. Petri, A. Capria, F. Berizzi, and M. Martorella, "High resolution and artifact cancellation in wideband DVB-T passive radar," in *Proc. 3rd FHR Focus Days PCL*, Wachtberg, Germany, 2011.

[9] C. R. Berger, B. Demissie, J. Heckenbach, P. Willett, and S. Zhou, "Signal processing for passive radar using OFDM waveforms," *IEEE J. Sel. Topics Signal Process.*, vol. 4, no. 1, pp. 226–238, Feb. 2010.

[10] G. Gassier, G. Chabriel, J. Barrre, F. Briolle, and C. Jauffret, "A unifying approach for disturbance cancellation and target detection in passive radar using OFDM," *IEEE Trans. Signal Process.*, vol. 64, no. 22, pp. 5959–5971, Nov. 2016.

[11] J. Neyman and E. Pearson, "On the problem of the most efficient test of statistical hypotheses," *Phil. Trans. Royal Soc. London*, vol. A 231, no. 9, pp. 289–337, 1933.

[12] H. V. Trees, *Detection, Estimation, and Modulation Theory*, 2nd ed. Hoboken, NJ, USA: Wiley, 2013.

[13] F. Colone, D. W. O'Hagan, P. Lombardo, and C. J. Baker, "A multistage processing algorithm for disturbance removal and target detection in passive bistatic radar," *IEEE Trans. Aerosp. Electron. Syst.*, vol. 45, no. 2, pp. 698–722, Apr. 2009.

[14] T. Cao, J. Palmer, and P. Berry, "False alarm control of CFAR algorithms with experimental bistatic radar data," in *Proc. IEEE Radar Conf.*, 2010, pp. 156–161.

[15] P. Falcone, F. Colone, A. Macera, and P. Lombardo, "Localization and tracking of moving targets with WiFi-based passive radar," in *Proc. IEEE Radar Conf.*, May 2012, pp. 0705–0709.

[16] M. Golabi, A. Sheikhi, and M. Biguesh, "A new approach for sea target detection in satellite based passive radar," in *Proc. 21st Iranian Conf. Elect. Eng.*, 2013, pp. 1–5.

[17] K. Bialkowski, I. Clarkson, and S. Howard, "Generalized canonical correlation for passive multistatic radar detection," in *Proc. IEEE Statist. Signal Process. Workshop*, 2011, pp. 417–420.

[18] A. Zaimbashi, M. Derakhtian, and A. Sheikhi, "GLRT-based CFAR detection in passive bistatic radar," *IEEE Trans. Aerosp. Electron. Syst.*, vol. 49, no. 1, pp. 134–159, Jan. 2013.

[19] J. Liu, H. Li, and B. Himed, "Two target detection algorithms for passive multistatic radar," *IEEE Trans. Signal Process.*, vol. 62, no. 22, pp. 5930–5939, Nov. 2014.

[20] S. P. Sira *et al.*, "Adaptive waveform design for improved detection of low-RCS targets in heavy sea clutter," *IEEE J. Sel. Topics Signal Process.*, vol. 1, no. 1, pp. 56–66, Jun. 2007.

[21] M. Glende, "PCL-signal-processing for sidelobe reduction in case of periodical illuminator signals," in *Proc. Int. Radar Symp.*, May 2006, pp. 1–4.

[22] S. Searle, J. Palmer, L. Davis, D. W. O'Hagan, and M. Ummenhofer, "Evaluation of the ambiguity function for passive radar with OFDM transmissions," in *Proc. IEEE Radar Conf.*, May 2014, pp. 1040–1045.

[23] M. Jarabo-Amores, M. Rosa-Zurera, R. Gil-Pita, and F. Lopez-Ferreras, "Study of two error functions to approximate the Neyman-Pearson detector using supervised learning machines," *IEEE Trans. Signal Process.*, vol. 57, no. 11, pp. 4175–4181, Nov. 2009.

[24] M.-P. Jarabo-Amores, D. d. la Mata-Moya, R. Gil-Pita, and M. Rosa-Zurera, "Radar detection with the Neyman–Pearson criterion using supervised-learning-machines trained with the cross-entropy error," *EURASIP J. Adv. Signal Process.*, vol. 2013, Mar 2013, Art. no. 44. [Online]. Available: http://dx.doi.org/10.1186/1687–6180-2013-44

[25] P. Gandhi and V. Ramamurti, "Neural networks for signal detection in non-Gaussian noise," *IEEE Trans. Signal Process.*, vol. 45, no. 11, pp. 2846–2851, Nov. 1997.

[26] D. Casasent and X. Chen, "Radial basis function neural network for nonlinear Fisher discrimination and Neyman-Pearson classification," *Neural Netw.*, vol. 16, pp. 529–535, 2003.

[27] D. Mata-Moya, M. Jarabo-Amores, and J. M. de Nicolás, "High order neural network based solution for approximating the averaged likelihood ratio," in *Proc. IEEE Stat. Signal Process. Workshop*, 2011, pp. 657–660.

[28] M. Davenport, R. Baraniuk, and C. Scott, "Tuning support vector machines for minimax and Neyman-Pearson classification," *IEEE Trans. Pattern Anal. Mach. Intell.*, vol. 32, no. 10, pp. 1888–1898, Oct. 2010.

[29] D. de la Mata-Moya, M. P. Jarabo-Amores, J. M. de Nicols, and M. Rosa-Zurera, "Approximating the Neyman–Pearson detector with 2C-SVMs. Application to radar detection," *Signal Process.*, vol. 131, pp. 364–375, 2017. [Online]. Available: http://www.sciencedirect.com/science/article/pii/S0165168416302079

[30] S. Haykin, "Cognitive radar: A way of the future," *IEEE Signal Process. Mag.*, vol. 23, no. 1, pp. 30–40, Jan. 2006.

[31] M. Inggs, "Passive coherent location as cognitive radar," in *Proc. Int. Waveform Diversity Des. Conf.*, Feb. 2009, pp. 229–233.

[32] U. Güntürkün, "Toward the development of radar scene analyzer for cognitive radar," *IEEE J. Ocean. Eng.*, vol. 35, no. 2, pp. 303–313, Apr. 2010.

[33] A. Farina, *Optimised Radar Processors*. Stevenage, U.K.: Peregrinus, 1987.

[34] V. Pidgeon, "Bistatic cross section of the sea," *IEEE Trans. Antennas Propag.*, vol. AP-14, no. 3, pp. 405–406, May 1966.

[35] C. Hightower, D. M. Maeschen, and C. A. Sanders-Foster, "Bistatic clutter phenomenological measurement/model development," SRS Technologies, Irvine, CA, USA, DARPA Order No. 5462, 1987.

[36] R. Larson *et al.*, "Bistatic clutter measurements," *IEEE Trans. Antennas Propag.*, vol. AP-26, no. 6, pp. 801–804, Nov. 1978.

[37] H. D. Griffiths *et al.*, "Measurement and modelling of bistatic radar sea clutter," *IET Radar Sonar Navigat. Spec. Issue Radar Clutter*, vol. 4, no. 2, pp. 280–292, 2010.

[38] M. Malanowski, R. Haugen, M. S. Greco, D. W. O'Hagan, R. Plsek, and A. Bernard, "Land and sea clutter from FM-based passive bistatic radars," *IET Radar, Sonar Navigat.*, vol. 8, no. 2, pp. 160–166, Feb. 2014.

[39] J. Brown *et al.*, "VHF airborne passive bistatic radar ground clutter investigation," in *Proc. IET Int. Conf. Radar Syst.*, 2012, pp. 1–5.

[40] M. Pola, P. Bezousek, and J. Pidanic, "Model comparison of bistatic radar clutter," in *Proc. Conf. Microw. Techn.*, 2013, pp. 182–185.

[41] A. D. Maio, G. Foglia, N. Pasquino, and M. Vadursi, "Measurement and analysis of clutter signal for GSM/DCS-based passive radar," in *Proc. IEEE Radar Conf.*, 2008, pp. 1–6.

[42] A. D. Maio *et al.*, "Measurement and comparative analysis of clutter for GSM and UMTS passive radar," *IET Radar, Sonar Navigat.*, vol. 4, no. 3, pp. 421–423, 2010.

[43] W. Al-Ashwal, K. Woodbridge, and H. Griffiths, "Analysis of bistatic sea clutter—Part I: Average reflectivity," *IEEE Trans. Aerosp. Electron. Syst.*, vol. 50, no. 2, pp. 1283–1292, Apr. 2014.

[44] W. A. Al-Ashwal, K. Woodbridge, and H. D. Griffiths, "Analysis of bistatic sea clutter—Part II: Amplitude statistics," *IEEE Trans. Aerosp. Electron. Syst.*, vol. 50, no. 2, pp. 1293–1303, Apr. 2014.

[45] R. Palam, M. Greco, P. Stinco, and F. Gini, "Analysis of sea spikes in NetRad clutter," in *Proc. 11th Eur. Radar Conf.*, Oct. 2014, pp. 109–112.

[46] R. Palam, M. S. Greco, P. Stinco, and F. Gini, "Statistical analysis of bistatic and monostatic sea clutter," *IEEE Trans. Aerosp. Electron. Syst.*, vol. 51, no. 4, pp. 3036–3054, Oct. 2015.

[47] M. Ritchie, A. Stove, K. Woodbridge, and H. Griffiths, "NetRad: Monostatic and bistatic sea clutter texture and doppler spectra characterization at s-band," *IEEE Trans. Geosci. Remote Sens.*, vol. 54, no. 9, pp. 5533–5543, Sep. 2016.

[48] P. Jarabo-Amores *et al.*, "IDEPAR: A multichannel DVB-T passive radar technological demonstrator in terrestrial radar scenarios," *IET Radar, Sonar Navigat.*, vol. 11, pp. 133–141, 2017.

[49] D. Mata-Moya, N. del Rey-Maestre, V. M. Peláez-Sánchez, M.-P. Jarabo-Amores, and J. M. de Nicolás, "MLP-CFAR for improving coherent radar detectors robustness in variable scenarios," *Expert Syst. Appl.*, vol. 42, no. 11, pp. 4878–4891, 2015. [Online]. Available: http://www.sciencedirect.com/science/article/pii/S0957417415000056

[50] T. Shan, S. Liu, Y. D. Zhang, M. G. Amin, R. Tao, and Y. Feng, "Efficient architecture and hardware implementation of coherent integration processor for digital video broadcast-based passive bistatic radar," *IET Radar, Sonar Navigat.*, vol. 10, no. 1, pp. 97–106, 2016.

[51] M. Ringer, G. Frazer, and S. J. Anderson, "Waveform analysis of transmitters of opportunity for passive radar," , Dept. Defence. Defence Sci. Technol. Org., Canberra, ACT, Australia, Tech. Rep. DSTO-TR-0809, Jun. 1999.

[52] H. V. Trees, *Detection, Estimation, and Modulation Theory—Part III: Radar-Sonar Processing and Gaussian Signals in Noise*. Hoboken, NJ, USA: Wiley, 2001.

[53] R. Saini and M. Cherniakov, "Investigation of Digital TV signal for Radar application," in *Proc. XI Eur. Signal Process. Conf.*, Toulouse, France, 2002, pp. 15–18.

[54] F. Colone, D. Pastina, P. Falcone, and P. Lombardo, "WiFi-based passive ISAR for high-resolution cross-range profiling of moving targets," *IEEE Trans. Geosci. Remote Sens.*, vol. 52, no. 6, pp. 3486–3501, Jun. 2014.

[55] J. Barcena-Humanes, J. Martin-de Nicolas, C. Solis-Carpintero, M. Jarabo-Amores, M. Rosa-Zurera, and D. Mata-Moya , "DVB-T ambiguity peaks reduction in passive radar applications based on signal reconstruction," in *Proc. 11th Eur. Radar Conf.*, Oct. 2014, pp. 597–600.

[56] S. Stein, "Differential delay/Doppler ML estimation with unknown signals," *IEEE Trans. Signal Process.*, vol. 41, no. 8, pp. 2717–2719, Aug. 1993.

[57] M. Skolnik, *Introduction to Radar Systems*, 3rd ed. New York, NY, USA: McGraw-Hill, 2002.

[58] E. Conte, M. Longo, and M. Lops, "Modelling and simulation of non-rayleigh radar clutter," *IEE Proc. F—Radar Signal Process.*, vol. 138, no. 2, pp. 121–130, Apr. 1991.

[59] V. Anastassopoulos and G. A. Lampropoulos, "Optimal CFAR detection in Weibull clutter," *IEEE Trans. Aerosp. Electron. Syst.*, vol. 31, no. 1, pp. 52–64, Jan. 1995.

[60] S. M. Kay, *Fundamentals of Statistical Signal Processing: Estimation Theory*, vol. I. Upper Saddle River, NJ, USA: Prentice-Hall, 1993.

[61] S. Atapattu, C. Tellambura, and H. Jiang, "A mixture gamma distribution to model the SNR of wireless channels," *IEEE Trans. Wireless Commun.*, vol. 10, no. 12, pp. 4193–4203, Dec. 2011.

[62] T. Hastie, R. Tibshirani, and J. Friedman, *The Elements of Statistical Learning: Data Mining, Inference, and Prediction* (Springer Series in Statistics), 2nd ed. New York, NY, USA: Springer, 2011.

[63] M. Liu, Y. Wu, Q. Zhao, and L. Gan, "SAR target configuration recognition using locality preserving projections," in *Proc. IEEE CIE Int. Conf. Radar*, 2011, vol. 1, pp. 740–743.

[64] J. Frank and J. Massey, "The Kolmogorov-Smirnov test for goodness of fit," *J. Amer. Statist. Assoc.*, vol. 46, no. 253, pp. 68–78, 1951.

[65] R. D'Agostino and M. Stephens, *Goodness of Fit Techniques*. New York, NY, USA: Marcel Dekker, 1986.

[66] T. Anderson, "On the distribution of the two-sample Cramér-von-Mises criterion," *Ann. Math. Statist. (Inst. Math. Statist.)*, vol. 6, no. 3, pp. 255–259, 1962.

[67] A. Farina, F. Gini, M. Greco, and L. Verrazzani, "High resolution sea clutter data: Statistical analysis of recorded live data," *IEE Proc.—Radar Sonar Navigat.*, vol. 144, pp. 121–130, 1997.

[68] S. D. Himonas and M. Barkat, "An adaptive CFAR signal detector for spatially correlated noise samples," in *Proc. 29th IEEE Conf. Decision Control*, Dec. 1990, vol. 6, pp. 3540–3545.

[69] G. McLachlan and D. Peel, *Finite Mixture Models*. Hoboken, NJ, USA: Wiley, 2000.

[70] J. A. Peacock, "Two-dimensional goodness-of-fit testing in astronomy," *Monthly Notices Royal Astronom. Soc.*, vol. 202, pp. 615–627, 1983.

[71] M. T. Hagan and M. B. Menhaj, "Training feedforward networks with the Marquardt algorithm," *IEEE Trans. Neural Netw.*, vol. 5, no. 6, pp. 989–993, Nov. 1994.

[72] J. C. Li, W. W. Y. Ng, P. P. K. Chan, and D. S. Yeung, "A growing architecture selection for multilayer perceptron neural network by the L-GEM," in *Proc. Int. Conf. Mach. Learn. Cybern.*, Jul. 2010, vol. 3, pp. 1402–1407.

Nerea del-Rey-Maestre received the M.Eng. degree in telecommunication engineering from the University of Alcalá, Alcalá de Henares, Spain, in 2012. Since 2011, she has been with the Department of Signal Theory and Communications, University of Alcalá. Her Ph.D. thesis is focused on the design and optimization of array signal processing and robust detection techniques in presence of spatial and temporal variable clutter in passive radar scenarios. Her research interests include the design and optimization of statistical signal processing and artificial-intelligence-based solutions in communications and radar systems applications.

María-Pilar Jarabo-Amores received the M.Eng. degree in telecommunication engineering from the Polytechnic University of Madrid, Madrid, Spain, in 1997, and the Ph.D. (Hons.) degree from the University of Alcalá, Alcalá de Henares, Spain, in 2005. She was an Assistant Professor from 1997 to 2003, a Lecturer from 2003 to 2008, and an Associate Professor since then, with the Department of Signal Theory and Communications, University of Alcalá. She has authored or coauthored more than 30 papers in international journals and more than 100 international conference papers. She has been involved in 25 international and national projects, in some of them as a Principal Investigator. She has supervised four Ph.D. thesis, one of them awarded by the Professional Telecommunication Association of Spain. Her research interests include statistical signal processing and artificial intelligence techniques in communications and radar systems.

David Mata-Moya received the M.Eng. degree in telecommunication engineering and the Ph.D. (Hons.) degree in electrical engineering from the University of Alcalá, Alcalá de Henares, Spain, in 2003 and 2012, respectively. Since 2004, he has been with the Department of Signal Theory and Communications, University of Alcalá. He has authored or coauthored more than 70 contributions to international journals and conferences. He has also been a member of the research team of several projects with public and private funding, including five projects funded by European agencies or the European Commission, four funded by the Spanish Ministry of Economy and Competitiveness, and four projects with ICT companies as a Principal Investigator. He has supervised one Ph.D. thesis. His research interests include statistical signal processing, artificial intelligence systems, signal models, radar signal processing, and radar system analysis and design.

José-Luis Bárcena-Humanes received the M.Eng. degree in telecommunication engineering and the Ph.D. (Hons.) degree in telecommunication engineering from the University of Alcalá, Alcalá de Henares, Spain, in 2010 and 2016, respectively. Since 2010, he has been with the Department of Signal Theory and Communications, University of Alcalá. His Ph.D. thesis dealt with the design and implementation of a technological passive radar demonstrator based on digital video broadcasting-terrestrial signals and the design of improved signal processing techniques for passive radar applications. His research interests include radar system analysis and design, radar signal processing, analysis of radar scenarios, and passive radar systems.

Pedro Gómez del Hoyo received the M.Eng. degree in telecommunication engineering from the University of Alcalá, Alcalá de Henares, Spain, in 2014. Since 2014, he has been with the Department of Signal Theory and Communications, University of Alcalá. His Ph.D. thesis is focused on the design of improved detection and tracking techniques in multistatic passive radar systems. His research interests include signal models, radar signal processing, radar system simulation, analysis, and design and detection, tracking, and data fusion techniques in multistatic radars.